LARGE-SCALE ICEBERG-TSUNAMI EXPERIMENTS

Valentin Heller (1), Tommaso Attili (2), Fan Chen (3), Markus Brühl (4), Roman Gabl (5), Xuexue Chen (6), Guido Wolters (7) & Helge Fuchs (8)

(1) University of Nottingham, UK, Email: valentin.heller@nottingham.ac.uk
(2) University of Nottingham, UK & University of Pisa, Italy, Email: t.attili@studenti.unipi.it
(3) University of Nottingham, UK, Email: fan.chen@nottingham.ac.uk
(4) Technische Universität Braunschweig, Germany, Email: m.bruehl@tu-braunschweig.de
(5) University of Edinburgh, UK & University of Innsbruck, Austria, Email: roman.gabl@ed.ac.uk
(6) Royal HaskoningDHV, The Netherlands, Email: xuexue.cheung@gmail.com
(7) Deltares, The Netherlands, Email: guido.wolters@deltares.nl
(8) ETH Zurich, Switzerland, Email: fuchs@vaw.baug.ethz.ch

Iceberg calving at outlet glaciers contributes to global sea-level rise in the context of climate change. This study investigates tsunamis generated by iceberg calving, so-called *iceberg-tsunamis*. Such tsunamis reached amplitudes of 50 m in the recent past and endanger human beings and coastal infrastructure. 73 unique large-scale experiments have been conducted in the 50 m ✗ 50 m Delta Basin at Deltares. These experiments involved the five iceberg calving mechanisms: A: capsizing, B: gravity-dominated fall, C: buoyancy-dominated fall, D: gravity-dominated overturning and E: buoyancy-dominated overturning. Gravity-dominated icebergs essentially fall into the water body whereas buoyancy-dominated icebergs essentially rise to the water surface. The iceberg-tsunamis from gravity-dominated mechanisms (B and D) are roughly an order of magnitude larger than from mechanisms A, C and E. The maximum wave heights and amplitudes and their decay with distance from the calving locations are correlated with six dimensionless parameters, with the Froude number, the relative iceberg width and the relative released energy identified as the most important ones. Empirical equations for initial iceberg-tsunami hazard assessment were derived predicting the wave features reasonably well, considering the variety of the underlying physics involved in the iceberg calving mechanisms. Ongoing and future work aims to analyse the wave parameters in more detail, investigate the wave features with a novel wave component decomposition method, compare iceberg- with landslide-tsunamis and investigate iceberg-tsunamis numerically.

1. INTRODUCTION

Iceberg calving accounts for a significant part of the mass losses of the Antarctic and Greenland Ice Sheets and contributes to global sea-level rise in the context of climate change (Hanna et al., 2013; Enderlin et al., 2014). Iceberg calving generates so-called *iceberg-tsunamis* (Heller et al., 2019). Significant iceberg-tsunamis have been observed in Greenland at the Eqip Sermia glacier where a wave amplitude of 50 m destroyed some infrastructure in 2014 (Lüthi & Vieli, 2016) and at the Helheim outlet glacier where approximately 25 km from the glacier front the measured wave was still 24 cm large (Vaňková & Holland, 2016). An iceberg-tsunami was also observed at the mountain glacier Tasman Glacier in New Zealand in 2011 (Dykes et al., 2016) and iceberg-tsunamis generated by capsizing icebergs destroyed a Greenlandic harbour in 1995 (N24, 2009).

Figure 1(a,b) shows iceberg calving events in nature. The icebergs interact with the surrounding water via different iceberg calving mechanisms (Benn et al., 2007; Heller et al., 2019; Massel & Przyborska, 2013; Minowa et al., 2018). Five idealised mechanisms have been investigated in this work as illustrated in Fig. 1(c): A: capsizing, B: gravity-dominated fall, C: buoyancy-dominated fall, D: gravity-dominated overturning and E: buoyancy-dominated overturning. Gravity-dominated icebergs essentially fall into the water body whereas buoyancy-dominated icebergs essentially rise to the water surface. The current understanding of iceberg-tsunamis is limited and only small-scale flume experiments (Burton et al., 2012) have been conducted thus far.

The tsunamigenic potentials of mechanisms A to E have been investigated within a HYDRALAB+ funded test campaign at Deltares in Delft. The five main objectives of the test campaign were (Heller, 2019):

I. Conduct large-scale iceberg-tsunami experiments in the 50 m × 50 m large Delta Basin under variation of the iceberg calving mechanisms (capsizing, fall, overturning) as well as the iceberg volume and kinematics

II. Quantify the tsunami features (height, length, velocity) and cross-compare the tsunamigenic potentials from the five different iceberg calving mechanisms

III. Relate the new findings to an established landslide-tsunami hazard assessment method to potentially transfer knowledge

IV. Analyse the new data using the highly promising new wave component decomposition method Korteweg-de Vries equations in combination with the nonlinear Fourier transform

V. Provide benchmark test cases to the numerical modelling community and apply the test cases to calibrate and validate numerical simulations of members of the project team to investigate additional iceberg-tsunami scenarios

This article provides a general overview about the experiments and presents some key results and empirical equations to predict the most relevant iceberg-tsunami parameters.
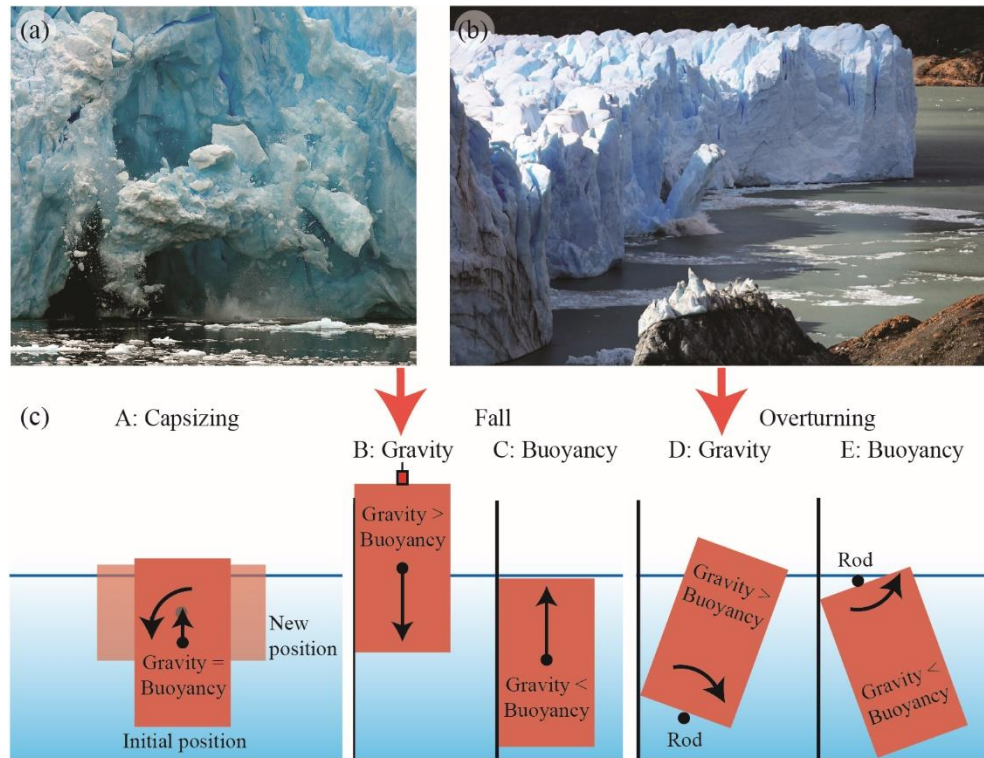

Figure 1: Real and idealised iceberg calving and iceberg-tsunami generation: (a) falling iceberg at Neko Harbour, Antarctica (courtesy of Alek Komarnitsky - www.komar.org), (b) overturning iceberg at Perito Moreno Glacier, Argentina (courtesy of Victor Qixiang Chen - http://photo.qyer.com/7259134/allphoto), (c) sketches of investigated idealised iceberg calving mechanisms from left to right: A: capsizing, B: gravity-dominated fall, C: buoyancy-dominated fall, D: gravity-dominated overturning and E: buoyancy-dominated overturning (Heller et al., 2019).

2. EXPERIMENTAL METHOD

2.1 Experimental Procedure

The experiments have been conducted under Froude similarity in the 50 m × 50 m basin shown in Fig. 2. Two blocks consisting of polypropylene homopolymer with a density similar to ice (≈920 kg/m^3) were released offshore (capsizing, Fig. 1c) and at the vertical boundary of the basin (fall, overturning, Figs. 1c and 2). The sizes of the two blocks were 0.800 m × 0.500 m × 0.500 m (block type 1) and 0.800 m × 0.500 m × 0.250 m (block type 2, Fig. 2) and they weighted up to 187 kg.

The experimental programme is shown in Table 1 and included 73 experiments (62 individual tests plus 11 repetitions) and two water depths h = 1.000 and 0.750 m. The capsizing mechanism

involved 16 experiments, the fall mechanism 30 (21 gravity- and 9 buoyancy-dominated), the overturning mechanism 20 (14 gravity- and 6 buoyancy-dominated) experiments and 7 fall experiments were conducted with a sphere, which will not be further addressed herein and are also excluded from the data analysis and specified parameter ranges. Videos of the experiments are included in Heller et al. (2019).
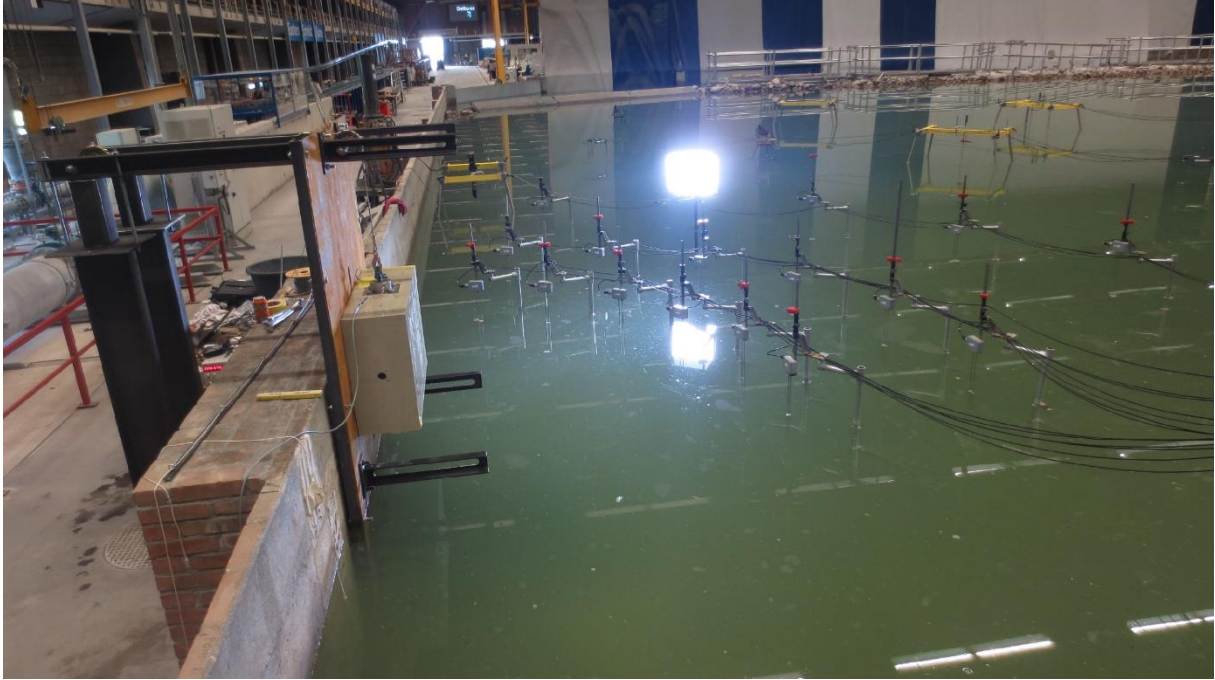

Figure 2: Picture of a gravity-dominated fall experiment (mechanism B) at the wall of the basin with block type 2 in the initial position and some of the 35 wave probes on the right-hand side.

Table 1: Experimental parameters of all 73 conducted experiments involving the five iceberg calving mechanisms A to E; the number of tests marked with $^+$ included repetitions. SWL = still water level and Neut. = Neutrally.

Block parameters	(i) Capsizing (mechanism A)			(iii) Overturning (mechanism D and E)			
Block release location	Offshore	Offshore	Offshore	At shore	At shore	At shore	At shore
Block type	1	2	2	1	2	2	2
Block length l (m)	0.800	0.800	0.500	0.800	0.800	0.500	0.500
Block width b (m)	0.500	0.500	0.800	0.500	0.500	0.800	0.800
Block thickness s (m)	0.500	0.250	0.250	0.500	0.250	0.250	0.250
Block volume V_s (m^3)	0.200	0.100	0.100	0.200	0.100	0.100	0.100
Block density ρ_s (kg/m^3)	929	924	924	936/923	912	912	936/912
Block mass m_s (kg)	185.8	92.4	92.3	187.1/184.6	91.2	91.2	93.6/91.2
Water depth h (m)	1.000	1.000	1.000	1.000	1.000	1.000	0.750
Release position above SWL (cm) (0 cm corresponds to the SWL)	Neut. buoyant	Neut. buoyant	Neut. buoyant	15, 0, −30, −60, −90	15, 0, −30, −60, −90	15, 0, −30, −60	15, 0, −30, −60
Number of runs (73 in total)	5$^+$	6$^+$	5$^+$	5	5	4	6$^+$

Block parameters	(ii) Fall (mechanism B and C)						
Block release location	At shore	At shore	At shore	At shore	At shore	At shore	At shore
Block type	1	2	1	1	2	2	sphere
Block length l (m)	0.800	0.800	0.500	0.500	0.500	0.500	0.215
Block width b (m)	0.500	0.500	0.800	0.800	0.800	0.800	0.215
Block thickness s (m)	0.500	0.250	0.500	0.500	0.250	0.250	0.215
Block volume V_s (m^3)	0.200	0.100	0.200	0.200	0.100	0.100	0.005
Block density ρ_s (kg/m^3)	936/923	936/912	936/923	936/923	936/912	936/912	922
Block mass m_s (kg)	187.1/184.6	93.6/91.2	187.1/184.6	187.1/184.6	93.6/91.2	93.6/91.2	4.8
Water depth h (m)	1.000	1.000	1.000	0.750	1.000	0.750	0.750
Release position above SWL (cm) (0 cm corresponds to the SWL)	0, −30, −60, −84	0, −30, −60, −83	30, 0, −30, −60, −70, −83	30, 0, −30, −60	30, 0, −30, −60, −83	30, 0, −30, −60	54, 32, 11, 0, −11, −32, −43
Number of runs (73 in total)	6$^+$	4	7$^+$	4	5	4	7

The experimental procedures for the five calving mechanisms (Fig. 1c) were as follows:

Capsizing (mechanism A in Fig. 1c): The blocks in the capsizing case were hold in position with a wooden rod guided through the centre of the blocks. This rod was hold in position on both sides with steel profiles and was able to move in the vertical direction (but not sideward or forward) and rotate. The rotation of the block was initiated in most cases by removing a fitting which stabilised the block. Block type 1 had to be slightly pushed by hand, with a force in the order of 1 N, to capsize. In some tests the blocks were pushed harder to investigate the effect of an increased rotation speed on the wave features.

Fall (mechanisms B and C in Fig. 1c): The blocks were hold in position with an electromagnet prior to release, which was connected to a rope as shown in Fig. 2. The supporting frame for this electromagnet and the blocks was fixed to a steel plate at the basin wall. The blocks were moved in vertical direction with a winch system which was fixed to a support structure outside the wave basin (Fig. 2). For the buoyancy-dominated fall case, the block was pulled under water with a rope attached to the centre of the block bottom to oppose the buoyancy force of up to 150 N. For some buoyancy-dominated tests the block had to be stabilised in addition with a steel beam from above and both the steel beam and the rope were then released simultaneously.

Overturning (mechanisms D and E in Fig. 1c): The blocks rotated around a fixed steel rod of 30 mm diameter. This rod was fed through two ball bearings fixed to the block surface. This ensured that the blocks underwent a pure rotation and no translation. The rod was hold in position on the sides with steel profiles (Fig. 2). The rod was located either below (gravity-dominated) or above (buoyancy-dominated) the block. For some buoyancy-dominated tests the block had to be stabilised in addition with a steel beam from above and the blocks started to move once the steel beam was removed.

2.2 Measurement System

The block kinematics was recorded with a sampling rate of ≈74 Hz with a 9 Degree of Freedom motion sensor (Adafruit BNO055). The sensor was located in a black enclosure and attached to the block surface. Two cameras (5 MP PointGrey ZBR2-PGEHD-50S5C-CS (which recorded at 15 Hz) and 2 MP IOIndustries Flare 2M280-CXP (at 100 Hz)) were used for general observations. The wave features were recorded at 100 Hz in different directions on one side of the block axis, given that the wave field is symmetric, with up to 35 resistance type wave probes.

Table 2: Name and locations of wave probes and cameras.

Iceberg calving mechanism	Device	Water depth h (m)	Locations in function of the radial distance r (m) and the wave propagation angle γ (°) (Fig. 3a,c)
Capsizing	Wave probes	1.000	A1 (2, 0); A10 (3, 0); A19 (5, 0); A28 (10, 0); A32 (15, 0); A2 (2, −15); A11 (3, −15); A20 (5, −15); A29 (10, −15); A3 (2, −30); A12 (3, −30); A21 (5, −30); A4 (2, −60); A13 (3, −60); A22 (5, −60); A5 (2, −90); A14 (3, −90); A23 (5, −90); A6 (2, −120); A15 (3, −120); A24 (5, −120); A7 (2, −150); A16 (3, −150); A25 (5, −150); A8 (2, −165); A17 (3, −165); A26 (5, −165); A30 (10, −165); A9 (2, −180); A18 (3, −180); A27 (5, −180); A31 (10, −180); A33 (15, −180)
Capsizing	Cameras	1.000	5 MP at 15 Hz: (6, −45); 2 MP at 100 Hz: (6, −95)
Fall/ overturning	Wave probes	1.000	B1 (2, 0); B7 (3, 0); B13 (5, 0); B19 (10, 0); B25 (15, 0); B31 (22.5, 0); B34 (35, 0); B2 (2, −15); B8 (3, −15); B14 (5, −15); B20 (10, −15); B26 (15, −15); B32 (22.5, −15); B35 (35, −15); B3 (2, −30); B9 (3, −30); B15 (5, −30); B21 (10, −30); B27 (15, −30); B33 (22.5, −30); B4 (2, −45); B10 (3, −45); B16 (5, −45); B22 (10, −45); B28 (15, −45); B5 (2, −60); B11 (3, −60); B17 (5, −60); B23 (10, −60); B29 (15, −60); B6 (2, −75); B12 (3, −75); B18 (5, −75); B24 (10, −75); B30 (15, −75)
Fall/ overturning	Wave probes	0.750	C1 (1.5, 0); C7 (2.25, 0); C13 (3.75, 0); C19 (7.5, 0); C25 (11.25, 0); C31 (16.875, 0); C34 (26.25, 0); C2 (1.5, −15); C8 (2.25, −15); C14 (3.75, −15); C20 (7.5, −15); C26 (11.25, −15); C32 (16.875, −15); C35 (26.25, −15); C3 (1.5, −30); C9 (2.25, −30); C15 (3.75, −30); C21 (7.5, −30); C27 (11.25, −30); C33 (16.875, −30); C4 (1.5, −45); C10 (2.25, −45); C16 (3.75, −45); C22 (7.5, −45); C28 (11.25, −45); C5 (1.5, −60); C11 (2.25, −60); C17 (3.75, −60); C23 (7.5, −60); C29 (11.25, −60); C6 (1.5, −75); C12 (2.25, −75); C18 (3.75, −75); C24 (7.5, −75); C30 (11.25, −75)
Fall/ overturning	Cameras	1.000 and 0.750	2 MP at 100 Hz: (6, −85); 5 MP at 15 Hz: (6, 45)

The coordinate origins of the cylindrical coordinate systems (r, z, γ) are shown in Fig. 3. The origins are located for all calving mechanisms in vertical direction z on the water surface. In the horizontal plan the origin is located at the block centre for the capsizing case (Fig. 3a) and at the front of the steel plate in the centre of the block in cross-shore direction for all other calving mechanisms (Fig. 3c). The wave propagation angle γ (angular angle) is defined positive in clockwise direction. The wave probes are numbered anti-clockwise starting at $\gamma = 0°$ and from smaller to higher radial distance r (Fig. 3a,c). Table 2 shows the locations of all wave probes.

The time in all experiments was adjusted such that $t = 0$ s corresponds to when the blocks started to move for experiments where they were initially in contact with the surrounding water, or when the blocks reached the water surface when they were initially located above the water body. The raw data of the motion sensor were further analysed in Matlab to transform the accelerations in global coordinates and to derive the block velocities and positions. The wave probe time series were individually shortened to remove data affected by reflection from the basin boundaries. The wave probe data were then filtered with a low-pass filter with a cut off frequency at 9 to 11 Hz. For wave probes A9, A17 and A25 in the capzising experiments and B21/C21, B24/C24 and B32/C32 for all fall and overturning experiments a low-pass filter with a cut off frequency at 3.0 or 3.5 Hz was applied to remove large high-frequency noise. For 3 locations out of all 2278 wave probe locations the wave probe signals remained noisy after filtering given that the waves were extremely small. These 3 data series were excluded from further analysis.
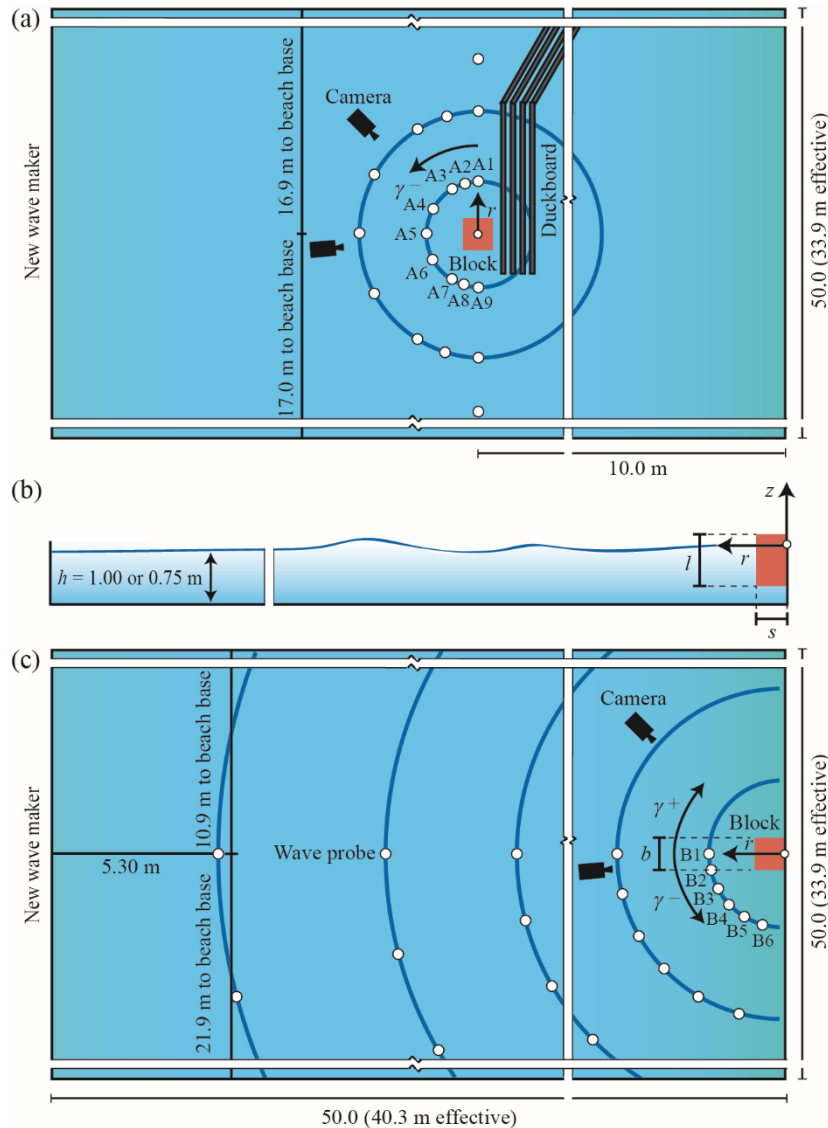

Figure 3: Sketches of experimental set-ups with some wave probes: (a) plan view of capsizing case, (b) side view of a gravity-dominated fall experiment and (c) plan view of a gravity-dominated fall experiment (Heller, 2019).

2.3 Governing Parameters

The following nine governing parameters were considered in the correlations of the iceberg-tsunami features such as the maximum wave heights and amplitudes and their decay with r and γ:

- Released energy E
- Water depth h
- Iceberg velocity V_s
- Iceberg thickness s
- Iceberg width b
- Iceberg volume V_s
- Iceberg density ρ_s
- Water density ρ_w
- Gravitational acceleration g

A wider variation of s and b was achieved by changing the orientation of the two block types 1 and 2 in the initial position (Table 1). The velocity V_s corresponds to the fastest moving section of the block and was derived based on the motion sensor data as 0.27 to 4.17 m/s over all block experiments. The density ρ_s changed slightly with the attachments to the block (Table 1). The additional parameter E was introduced after the test campaign varying between 6 and 980 J over all block experiments making this parameter instrumental to correlate very large and very small waves. This energy corresponds to the energy difference of the iceberg between the initial and final positions and is thus the maximum available energy to be transferred into tsunami energy. The theoretical expressions and values for E were derived by Heller et al. (2019) in function of the iceberg calving mechanism, iceberg geometry and initial position relative to the water surface.

The nine governing parameters can be expressed in dimensionless form based on the reference quantities g, h and ρ_w. This results in the following six dimensionless parameters and ranges covered by the block experiments (Attili, 2019):

- Relative released energy: $0.0006 \leq E_r = E/(\rho_w g h^4) \leq 0.3157$
- Froude number: $0.09 \leq F = V_s/(gh)^{1/2} \leq 1.33$
- Relative iceberg thickness: $0.25 \leq S = s/h \leq 0.67$
- Relative iceberg width: $0.50 \leq B = b/h \leq 1.07$
- Relative iceberg volume: $0.10 \leq V = V_s/h^3 \leq 0.47$
- Relative density: $0.91 \leq D = \rho_s/\rho_w \leq 0.94$

Scale effects due to the kinematic viscosity ν_w and surface tension σ_w were neglected in this Froude scaling experiments given that the Weber number $W = \rho_w g h^2/\sigma_w \geq 75{,}552$ and Reynolds number $R = g^{1/2}h^{3/2}/\nu_w \geq 2{,}033{,}835$ in the experiments were large and satisfied the limitations $W \geq 5{,}000$ and $R \geq 300{,}000$ applicable for the physically closely related subaerial landslide-tsunamis (Heller et al., 2008). The absolute and relative measurement errors of most dimensional and dimensionless parameters are given in Heller et al. (2019). The six dimensionless parameters are used in the *Results and Discussion* section to correlate the maximum wave heights and amplitudes.

3.   RESULTS AND DISCUSSION

Figure 4 shows the free water surface η versus time t of five selected experiments involving all five iceberg calving mechanisms. These wave profiles were all measured at relative radial distance r/h = 2 (Fig. 3 and Table 2). The scales on the y-axes in Fig. 4 vary by up to a factor of 20. The wave magnitudes significantly differ for the mechanisms A to E; the gravity-dominated overturning mechanism D results in the largest tsunamis followed by the gravity-dominated fall mechanism B. The three remaining mechanisms resulted in up to a factor of 27 smaller waves (Heller et al., 2019). Further, the wave trains consist of several nonlinear waves for all mechanisms, similar as for subaerial landslide-tsunamis (Heller & Spinneken, 2015). The largest wave amplitude is observed in the middle of the wave train for the slower moving mechanisms A, C and E. For the gravity-dominated mechanisms B and D the largest wave is observed earlier in the wave train.

Figure 5 shows the relative maximum wave heights (Fig. 5a) and the relative maximum wave amplitudes (Fig. 5b) for all 66 block experiments and iceberg calving mechanisms combined in function of the six dimensionless parameters. The best correlations were found with a regression analysis based on the least-square approach with the Matlab function *lsqcurvefit*. Some restrictions

were imposed on the exponents (e.g. > 0) to obtain physical meaningful results. The corresponding empirical equations and coefficients of determination R^2 are

$$\frac{H_M}{h} = 0.26(E_r^{0.20}F^{1.72}S^{0.53}B^{1.10}V^{0.20}D^{0.10})^{0.50} \qquad (R^2 = 0.92) \qquad (1)$$

$$\frac{a_M}{h} = 0.14(E_r^{0.20}F^{2.07}S^{0.10}B^{1.20}V^{0.20}D^{0.40})^{0.50} \qquad (R^2 = 0.91) \qquad (2)$$

The most important parameter in Eqn. (1) and (2) is F with an exponent of approximately 2. Further important are the relative slide width B, with an exponent slightly larger than 1, as well as E_r. E_r is influential due to the combination of the exponent 0.20 with the large range of E_r over nearly three orders of magnitude. The influences of S, V and D on the maximum wave parameters are significantly smaller. Figure 5 confirms that the tsunami heights generated by mechanisms B and D (gravity-dominated) were roughly an order of magnitude larger than for mechanisms A, C and E over all conducted experiments. Most data lie within the ±40% bounds, however, the inserts in Fig. 5 reveal that Eqn. (1) and (2) tend to overpredict the buoyancy-dominated and capsizing mechanisms and therefore operate on the save side.
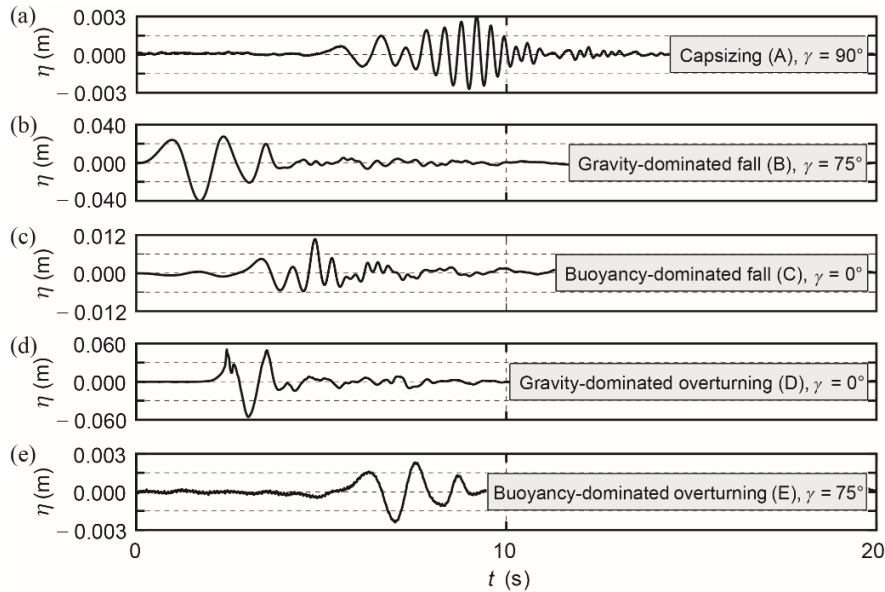

Figure 4: One selected iceberg-tsunami profile for each calving mechanism A to E. These tsunami profiles were recorded at ($r/h = 2$, γ) where the maximum wave height H_M was measured. (a) Capsizing, (b) gravity-dominated fall, (c) buoyancy-dominated fall, (d) gravity-dominated overturning and (e) buoyancy-dominated overturning mechanism. The scales on the y-axes change by up to a factor of 20 (Heller et al., 2019).
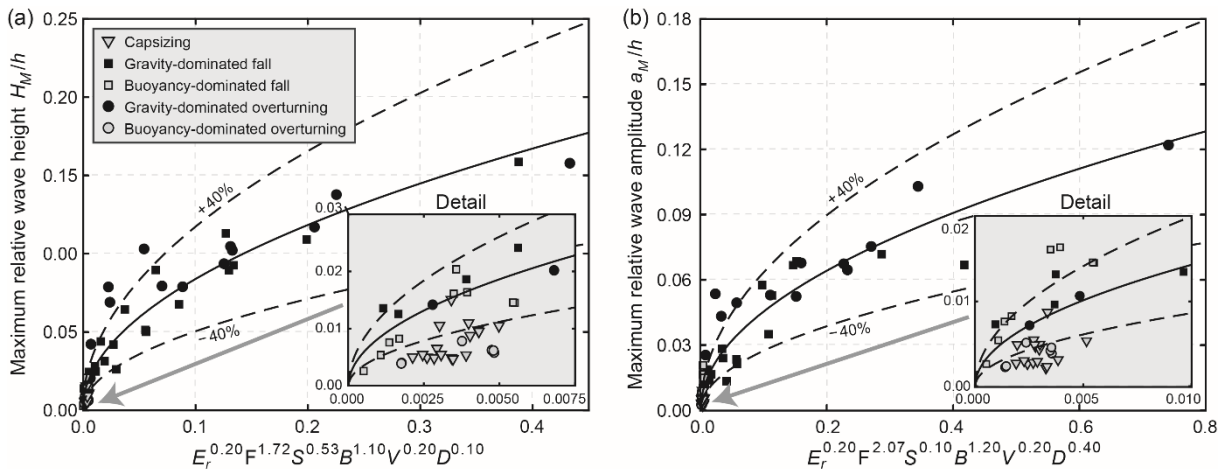

Figure 5: Maximum wave parameters for all calving mechanisms: (a) maximum relative wave height H_M/h versus a combination of the dimensionless parameters and Eq. (1) plotted as (—) with ±40% deviation as (- -) ($R^2 = 0.92$) and (b) maximum relative wave amplitude a_M/h versus a combination of the dimensionless parameters and Eq. (2) plotted as (—) with ±40% deviation as (- -) ($R^2 = 0.91$). The inserts show the smallest waves in more detail.
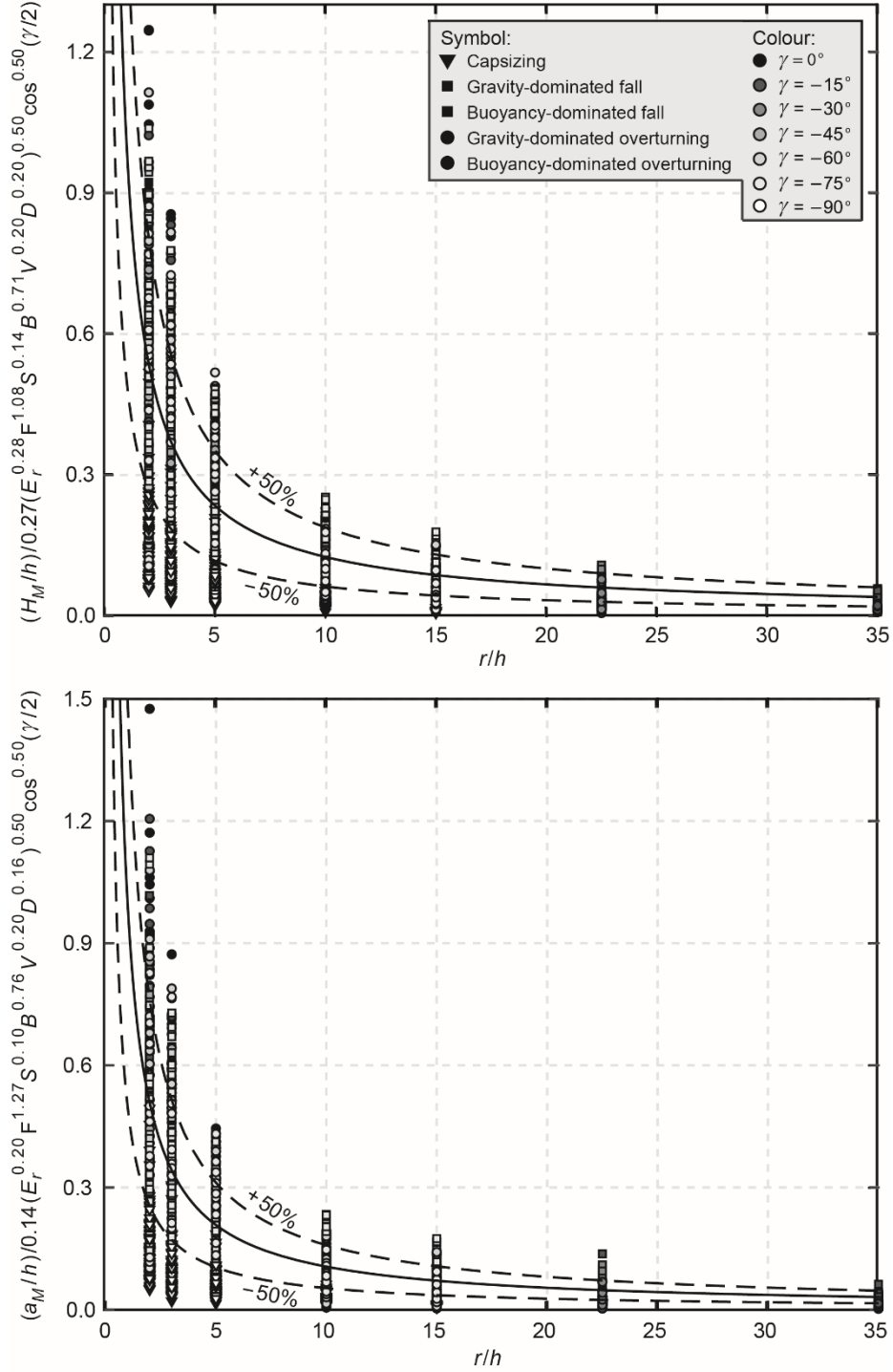
Figure 6: Maximum wave parameter decays for all calving mechanisms: (a) normalised wave heights versus the relative distance r/h and Eq. (3) plotted as (—) with ±50% deviation as (--) ($R^2 = 0.80$) and (b) normalised wave amplitude versus the relative distance r/h and Eq. (4) plotted as (—) with ±50% deviation as (--) ($R^2 = 0.78$).

The decays of the relative maximum wave heights and amplitudes for all 66 block experiments and iceberg calving mechanisms combined are represented by

$$\frac{H_M}{h}\left(\frac{r}{h},\gamma\right) = 0.27(E_r^{0.28}\mathrm{F}^{1.08}S^{0.14}B^{0.71}V^{0.20}D^{0.20})^{0.50}\left(\frac{r}{h}\right)^{-0.90}\cos^{0.5}\left(\frac{\gamma}{2}\right) \qquad (R^2 = 0.80) \qquad (3)$$

$$\frac{a_M}{h}\left(\frac{r}{h},\gamma\right) = 0.14(E_r^{0.20}\mathrm{F}^{1.27}S^{0.10}B^{0.76}V^{0.20}D^{0.16})^{0.50}\left(\frac{r}{h}\right)^{-0.98}\cos^{0.5}\left(\frac{\gamma}{2}\right) \qquad (R^2 = 0.78) \qquad (4)$$

The parameters F, B and E_r are also dominant in Eqn. (3) and (4) and S, V and D play a less significant roll. The wave decay is close to $(r/h)^{-1.0}$, corresponding both to the theoretically expected decay for a wave created by a point source propagating on a spatial water surface (Kranzer & Keller, 1959) and the decay previously found for landslide-tsunami experiments conducted in a wave basin (Heller & Spinneken, 2015). Figure 6 represents these empirical correlations. It shows the relative wave heights H_M/h and amplitudes a_M/h divided by the dimensionless parameter combinations of Eqn. (3) and (4) on the *y*-axes versus the relative distance r/h on the *x*-axes. The data follow the predictions based on Eqn. (3) and (4) reasonably well, considering the variety of underlying physics involved in the five iceberg calving mechanisms. However, the data scatter is particularly large in proximity of the iceberg calving location where water splashes reached the wave probes at $r/h = 2$ in some of the experiments.

4.   CONCLUSIONS AND OUTLOOK

Unique large-scale experiments have been conducted in the 50 m × 50 m Delta Basin at Deltares within a HYDRALAB+ test campaign. 73 iceberg-tsunami experiments with up to 187 kg heavy blocks under variation of the iceberg volume, geometry, kinematics and initial position relative to the water surface have been conducted. The blocks interacted with the surrounding water through five iceberg calving mechanisms namely: A: capsizing, B: gravity-dominated fall, C: buoyancy-dominated fall, D: gravity-dominated overturning and E: buoyancy-dominated overturning. The main conclusions of this study are summarised as follows:

- The tsunami magnitudes generated by mechanisms B and D (gravity-dominated) are roughly an order of magnitude larger than from mechanisms A, C and E. Icebergs of a given volume and geometry released above the water surface are therefore significantly more hazardous in terms of tsunami generation than neutrally buoyant icebergs or icebergs released underwater.

- The tsunami features were expressed in function of six dimensionless parameters where the Froude number F, the relative iceberg width B and the relative released energy E_r are the most dominant ones.

- Empirical equations for the maximum wave heights and amplitudes and their decay with propagation distance r and wave propagation angle γ are presented which are useful for initial iceberg-tsunami hazard assessment.

Ongoing and future work aims to resolve all objectives (I) to (V) mentioned in the *Introduction* by correlating the wave parameters for each iceberg calving mechanism individually (Attili, 2019) and by applying the highly promising new wave component decomposition method Korteweg-de Vries equations in combination with the nonlinear Fourier transform to iceberg-tsunamis (Brühl & Becker, 2018). The iceberg-tsunamis will also be compared in more detail with landslide-tsunamis (Heller & Spinneken, 2015) and a numerical model is under development which, in principle, is capable of simulating all five iceberg calving mechanisms and iceberg-tsunamis (Chen et al., 2019).

ACKNOWLEDGEMENT

REFERENCES

Attili, T. (2019). Analysis of iceberg-tsunamis from large-scale experiments. *MSc thesis*. University of Pisa, Italy.

Benn, D.I., Warren, C.R. and Mottram, R.H. (2007). Calving processes and the dynamics of calving glaciers. *Earth-Science Reviews* 82, 143-179.

Burton, J.C., Amundson, J.M., Abbot, D.S., Boghosian, A., Cathles, L.M., Correa-Legisos, S., Darnell, K.N., Guttenberg, N., Holland, D.M. and MacAyeal, D.R. (2012). Laboratory

investigations of iceberg capsize dynamics, energy dissipation and tsunamigenesis. *Journal of Geophysical Research* 117(F01007).

Brühl, M. and Becker, M. (2018). Analysis of subaerial landslide data using nonlinear Fourier transform based on Korteweg-deVries equations (KdV-NLFT). *Journal of Earthquake and Tsunami* 12(2), 1-21.

Chen, F., Heller, V. and Briganti, R. (2019). Numerical modelling of tsunamis generated by iceberg calving validated with large-scale laboratory experiments (in preparation).

Dykes, R.C., Brook, M.S. and Lube, G. (2016). A major ice-calving event at Tasman Glacier terminus, Southern Alps, 22 February 2011. *Journal of the Royal Society of New Zealand* 47(4), 336-343.

Enderlin, E.M., Howat, I.M., Jeong, S., Noh, M.-J., van Angelen, J.H. and van den Broeke, M.R. (2014). An improved mass budget for the Greenland ice sheet. *Geophysical Research Letters* 41, 866-872.

Hanna, E., Navarro, F.J., Pattyn, F., Domingues, C.M., Fettweis, X., Ivins, E.R., Nicholls, R.J., Ritz, C., Smith, B., Tulaczyk, S., Whitehouse, P.L. and Zwally, H.J. (2013). Ice-sheet mass balance and climate change. *Nature* 498, 51-59.

Heller, V. (2019). Tsunamis due to ice masses - Different calving mechanisms and linkage to landslide-tsunamis – Data storage report. *Data storage report of HYDRALAB+ test campaign* (online http://hydralab.eu/research--results/ta-projects/project/hydralab-plus/11/, 10.5281/zenodo.2556614).

Heller, V., Chen, F., Brühl, M., Gabl, R., Chen, X., Wolters, G. and Fuchs, H. (2019). Large-scale experiments into the tsunamigenic potential of different iceberg calving mechanisms. *Scientific Reports* 9:861.

Heller, V., Hager, W.H. and Minor, H.-E. (2008). Scale effects in subaerial landslide generated impulse waves. *Experiments in Fluids* 44(5), 691-703.

Heller, V. and Spinneken, J. (2015). On the effect of the water body geometry on landslide-tsunamis: physical insight from laboratory tests and 2D to 3D wave parameter transformation. *Coastal Engineering* 104(10), 113-134.

Kranzer, H.C. and Keller, J.B. (1959). Water waves produced by explosions. *Journal of Applied Physics* 30(3), 398-407.

Lüthi, M.P. and Vieli, A. (2016). Multi-method observation and analysis of a tsunami caused by glacier calving. *The Cryosphere* 10, 995-1002.

Massel, S.R. and Przyborska, A. (2013). Surface wave generation due to glacier calving. *Oceanologia* 55(1), 101-127.

Minowa, M., Podolskiy, E.A., Sugiyama, S., Sakakibara, D. and Skvarca, P. (2018). Glacier calving observed with time-lapse imagery and tsunami waves at Glaciar Perito Moreno, Patagonia. *Journal of Glaciology* 64(245), 362-376.

N24 (2009). Tsunami Greenland - Tsunami Groelândia 1995. Online under https://www.youtube.com/watch?v=z8LWSOPwkn8 (in German).

Vaňková, I. and Holland, D.M. (2016). Calving signature in ocean waves at Helheim Glacier and Sermilik Fjord, East Greenland. *Journal of Physical Oceanography* 46(10), 2925-2941.